Spin-orbit effects in the photoionization excitation of neon

T. W. Gorczyca
Department of Physics, Western Michigan University, Kalamazoo, Michigan 49008

Z. Felfli
Center for Theoretical Studies of Physical Systems, Clark Atlanta University, Atlanta, Georgia 30314

H.-L. Zhou and S. T. Manson
Department of Physics and Astronomy, Georgia State University, Atlanta, Georgia 30303
(Received 26 May 1998)

Using multichannel quantum-defect theoretical methods, we have performed highly correlated R-matrix calculations for the photoionization excitation of neon in the (50–53)-eV photon energy range, where numerous doubly excited resonances are found. By incorporating spin-orbit effects through an intermediate-coupling frame transformation, we have reproduced experimental observance of the significant breakdown of LS coupling in resonant angular distributions and fine-structure partial cross sections. Extreme sensitivity to the target structure in this weak process and strong interactions between neighboring Rydberg series of resonances make a detailed comparison for every resonance difficult, but many of the interesting spin-orbit features, beyond fine-structure splitting of series, are revealed. This method permits a quantitative analysis of LS-forbidden contributions to complex photoionization spectra and should prove useful for studying spin-orbit effects in light atomic systems. [S1050-2947(98)02711-5]

PACS number(s): 32.80.Fb

I. INTRODUCTION

With the advent of third-generation synchrotron radiation facilities and recent improvements in their resolution [1], it is now possible to study higher-order photoionization processes in greater experimental detail. Among these are two-electron processes, which require going beyond the single-electron picture and considering further the interaction between atomic electrons.

Helium, being the simplest two-electron system, has been studied extensively, both theoretically and experimentally [2], followed by lithium, with three electrons, which is also receiving considerable attention, due in part to the ''hollow states'' observed [3]. While more complicated, lithium is still fairly tractable by theoretical methods using a large basis set. Various other quasi-two-electron atoms have been studied, most notably the alkaline-earth atoms Be, Mg, Ca, Sr, and Ba [4], where the core was described by a model potential. In all of these cases except lithium, however, only two electrons are treated.

Since neon is the next rare-gas atom after helium, it has been studied nearly as extensively [1]. Even though Codling, Madden, and Ederer were able to delineate numerous doubly excited resonances above the first excitation threshold 30 years ago [5], there has been very little theoretical work done in this higher-energy region due to the extreme complexity of these states. The R-matrix calculations by Burke and Taylor [6] studied the two lowest $2s2p^6np$ resonances seen in the $2s^22p^5$ photoionization continuum; Taylor [7] subsequently extended that treatment to the angular distribution parameter of the same resonances. However, they did not consider two-electron resonances (where two electrons are photoexcited out of the ground state). The earliest measurements and classification of resonances in neon by Codling *et al.* [5] were already aware that the lowest resonance $2s^22p^43s3p$ is in fact two-electron in nature. This particular resonance was later studied using a close-coupling method [8]. At higher photon energies above the $2s2p^6np$ Rydberg limit, numerous other doubly excited $2s^22p^43lnl'$ resonances exist, but it is only recently that there has been any theoretical investigation of the resonances in this region [9]. Unlike the quasi-two-electron systems of the alkaline-earth elements, doubly excited states in neon are further complicated by the open $2p^4$ subshell, which has three different LS couplings ($^3P,^1D,^1S$) and therefore three times as many resonances for a given set of outer-electron quantum numbers $nln'l'$.

Spurred by the latest improvements in the experimental photon energy resolution at synchrotron facilities and the subsequent detailed results, theoretical (R-matrix) studies have recently been performed for neon. In a highly detailed joint theoretical and experimental study [9], the R-matrix method, together with multichannel quantum-defect theory and an LS-jj frame transformation, was shown to reproduce the experimental features in the photon energy range from 44 to 53 eV. However, in that experiment, only the *total* photoionization cross section was determined, so the corresponding theoretical treatment did not report partial cross sections or photoelectron angular distributions. Nevertheless, certain spin-orbit effects were noticeable in the experiment and predicted by the LS-jj recoupling frame transformation method, in particular, the fine-structure splitting of Rydberg series.

Another recent joint experimental and theoretical study of neon determined not only the total photoionization cross section but also the photoelectron angular distribution [10]. A standard LS-coupled R-matrix method was shown to reproduce the observed resonance features for the entire $2s2p^6nl$

Rydberg region (44–49 eV) and the lower-lying $2s^2 2p^4 3s3p$ resonance. A follow-up experimental study, which looked at higher energies, resolved the individual *partial* photoionization-excitation cross sections as well as the angular distributions of electrons [11]. Different and prominent spin-orbit induced features were revealed, namely, the appearance of 0° photoelectrons and the nonconstant ratio of the fine-structure partial cross sections. Both of these LS-forbidden features were observed in the transition to the parity-unfavored $2s^2 2p^4(^3P)3s(^2P)\epsilon p$ photoionization-excitation continuum. While simple perturbative calculations were able to qualitatively confirm the spin-orbit mixing responsible for this LS-forbidden behavior, a quantitative analysis of this system demands a more rigorous treatment, such as in the earlier R-matrix calculations [9,10]. Higher-order correlation effects must be included in order to accurately describe the complex, doubly excited resonances of interest and, furthermore, spin-orbit effects are required for the investigation of LS-coupling breakdown. This system therefore presents a formidable test on the accuracy of R-matrix methods in describing complex spectra.

The purpose of the present theoretical study is to perform highly correlated R-matrix calculations, with the inclusion of spin-orbit effects, for the $h\nu + 2s^2 2p^6 \rightarrow 2s^2 2p^4(^3P)3s(^{2,4}P)\epsilon p(\epsilon f)$ photoionization excitation of neon, that are differential in the photoelectron's angle and kinetic energy. We will restrict our investigation to the region where LS-forbidden resonance behavior was observed (50.5–53.1 eV) [11]. In order to do this, we have restructured the Belfast R-matrix codes [12] by implementing multichannel quantum-defect theoretical (MQDT) and frame transformation methods, following closely in spirit the earlier eigenchannel R-matrix studies [4,9]. However, an additional and important feature is the inclusion of term coupling, that is, the spin-orbit interaction between LS-coupled ionic target states. These improvements to the Belfast R-matrix codes will be outlined in the next section, along with a description of the atomic orbitals, target states, and configurations used. A discussion concerning the quantification of spin-orbit-induced features in terms of the angular momentum transfer is presented in Sec. III. Results are then presented for partial photoionization cross sections and angular distribution parameters in Sec. IV, where we demonstrate the degree of spin-orbit mixing and compare to the LS-forbidden experimental results. Concluding remarks follow in Sec. V.

II. THEORETICAL METHODS

A. Wave-function considerations

A lot of light can be shed on the important aspects of treating doubly excited resonances, as far as the present study of spin-orbit features in the photoionization excitation of neon is concerned, by first considering the form of the R-matrix wave function. It is expanded in a basis as [13]

$$\Psi_k = \mathcal{A} \sum_i \Phi_i(R) \sum_j c_{ijk} u_{ij}(r) + \sum_\alpha d_{\alpha k} \chi_\alpha(R,r). \quad (1)$$

Here R stands for the collective coordinates of the target ion electrons, Φ_i are wave functions for the target ionic states (the outer electron's spin and angular momenta are implicitly coupled to this), the $u_{ij}(r)$ are basis functions for the outer (''continuum'' or ''Rydberg'') electron's orbital, $\mathcal{A}$ is an antisymmetrization operator, and the coefficients c_{ijk} and $d_{\alpha k}$ are later determined from variational considerations. The target wave functions Φ_i are linear combinations of configurations ϕ_k, a configuration-interaction (CI) expansion, formed by coupled Slater determinants of atomic orbitals

$$\Phi_i(R) = \sum_m U_{im} \phi_m(R) \quad \text{or} \quad \mathbf{\Phi} = \mathbf{U}\phi. \quad (2)$$

The coefficients U_{im} form a unitary matrix that diagonalizes the ionic Hamiltonian within the basis Φ_i:

$$\langle \Phi_{i'} | \mathcal{H}(\mathrm{Ne}^+) | \Phi_i \rangle = E_i \delta_{ii'} \quad \text{or} \quad \mathbf{U}^\dagger \mathbf{H} \mathbf{U} = \mathbf{E}, \quad (3)$$

where $\mathbf{E}$ is a diagonal matrix of ionic eigenenergies. The χ_α are additional basis configurations constructed from only the target atomic orbitals, so they are completely contained within the R-matrix ''box.'' Their inclusion is necessary to compensate for the restriction that the $u_{ij}(r)$ are orthonormal to all target orbitals making up the target states and to include further correlation. More importantly, they are quite relevant to the present study in that many of the complex low-lying resonances are described almost completely by these basis functions. For a given basis Ψ_k, the neon Hamiltonian is then diagonalized to determine the R-matrix poles and surface amplitudes [13]:

$$\langle \Psi_{k'} | \mathcal{H}(\mathrm{Ne}) | \Psi_k \rangle = \epsilon_k \delta_{kk'}. \quad (4)$$

Ideally, we would like to include the spin-orbit operator in the Hamiltonian of Eq. (4) for our R-matrix calculation. Due to the prohibitively large storage needed to perform the present highly correlated calculations and the increase in computational effort by orders of magnitude in order to diagonalize the Hamiltonian in Eq. (4), we have chosen instead to neglect the spin-orbit operator at this stage, solve for each $J = 1^o$ LS-coupled R-matrix separately, and then use an intermediate-coupling frame transformation method, which we describe next.

B. Intermediate-coupling frame transformation method

One of the effects of the spin-orbit interaction in the scattering of electrons from Ne^+ ions is the energy splitting of levels; continuum or Rydberg orbitals coupled to energetically different fine-structure target levels propagate with different wave numbers and their phase accumulation may differ. As a result, linear superpositions of initial waves of one LS symmetry can populate other LS symmetries of the same J. Outside of the R-matrix box, this difference can be included through a frame transformation [4,14–16], which consists of recoupling from our LS coupling to some other appropriate coupling scheme that includes the core total angular momentum J_c as an intermediate quantum number, followed by adjusting the core energies to the experimentally observed fine-structure energies, thereby varying the otherwise equal phases of the different fine-structure continua. When this transformation is performed on MQDT scattering quantities, where all channels are initially regarded as open,

TABLE I. Ne and Ne^+ configurations included.

ϕ_m		χ_α	
Basic configuration	Allowed promotions	Basic configuration	Allowed promotions
$2s^22p^5$	2	$2s^22p^6$	3
$2s2p^6$	2	$2s^22p^43s3p$	2
		$2s^22p^43p3d$	2
Symmetry	Number of configurations	Symmetry	Number of configurations
$^2P^o$	125	^1S	587
^2S	60	$^1P^o$	1386
^4P	80	$^3S^o$	916
^2P	110	$^3P^o$	2317
$^4P^o$	72	$^3D^o$	2720
^2D	93		
$^4D^o$	76		
$^2D^o$	110		
$^2S^o$	42		
$^4S^o$	38		
$^2F^o$	75		

the differing phase accumulations, and therefore the spin-orbit mixing, can occur for closed channels describing the resonances as well as open channels describing the continua. We point out that although the recoupling approach is routinely used in conjunction with the Belfast codes via the program JAJOM [17–19], that transformation is only for open channels and is not used with MQDT quantities.

1. LS coupling

The frame transformation approach was introduced into the Belfast R-matrix codes [12] as follows. An LS-coupled R-matrix calculation was performed for each LS partial wave that couples to the desired final symmetry $J=1^o$, namely, the $^1P_1^o$, $^3S_1^o$, $^3P_1^o$, and $^3D_1^o$ waves [one is also performed for the $^1S_1$ initial wave of the ground state and the (one column) dipole matrix $\mathbf{d}$ from this state to the $^1P^o$ symmetry is computed]. All channels are initially treated as open, i.e., linear combinations of the inner R-matrix solutions $\mathbf{F}^{in}$ are matched to the regular ($\mathbf{S}$) and irregular ($\mathbf{C}$) Coulomb functions regardless of channel energy:

$$\mathbf{F}^{in}\mathbf{A}=\mathbf{S}+\mathbf{C}\mathbf{K}^{LS}, \tag{5}$$

where $\mathbf{A}$ is the matrix of coefficients of this linear expansion for each independent solution. For positive channel energies, the elements of the diagonal matrices are just the regular and (negative) irregular Coulomb functions analytic in the energy; for negative energy channels, both functions diverge, rendering them physically meaningless. Unphysical reactance matrices $\mathbf{K}^{LS}$ are thus produced, which nevertheless give the effective interactions between all channels; for now they are denoted by $[(L_cl)L][(S_cs)S]J$, the orbital and spin angular momenta of the ionic core, outer electron, and Ne system, respectively ($J=1^o$ is the only allowed *total* angular momentum for our case since the ground state of Ne has total angular momentum $J_0=0$). The unphysical dipole matrix $\mathbf{d}$, chosen for now to have (unphysical) K-matrix normalization, only couples the $^1S_1$ ground state to the LS-allowed $^1P_1^o$ final scattering state. Therefore, in the absence of any spin-orbit effects, the other final partial waves do not contribute to the photoionization cross section.

2. LS-J_{cs} recoupling

To include spin-orbit effects, we have chosen a J_{cs}-coupling scheme given by $\{[(L_cS_c)J_cs]J_{cs}l\}J$. This coupling is particularly useful since, for the present case, the intermediate angular momentum J_{cs} is identical to the angular momentum transfer j_t and, as we shall see, certain LS-forbidden contributions to the cross section can be identified by this value. The $J=1$ unphysical reactance matrix is related to the (block-diagonal) LS-coupled one by the unitary transformation

$$\mathbf{K}^{J_{cs}}=\mathbf{X}^\dagger\mathbf{K}^{LS}\mathbf{X}, \tag{6}$$

where the elements of the unitary matrix $\mathbf{X}$ are the LS-J_{cs} recoupling coefficients [20]

$$\begin{aligned}\{\mathbf{X}\}_{\gamma\delta}&=\langle[(L_cl)L(S_cs)S]J|\{[(L_cS_c)J_cs]J_{cs}l\}J\rangle\\&=(-1)^{2J_{cs}+L_c+S_c+s+S+l+L}[J_c][S][J_{cs}][L]\\&\times\begin{Bmatrix}L_c & S_c & J_c\\ s & J_{cs} & S\end{Bmatrix}\begin{Bmatrix}S & L_c & J_{cs}\\ l & J & L\end{Bmatrix}\end{aligned} \tag{7}$$

and $\gamma\leftrightarrow[(L_cl)L(S_cs)S]J$ and $\delta\leftrightarrow[(L_cS_c)J_cs]J_{cs}l\}J$ are the channel indices for the LS and J_{cs} schemes, respectively. Quantities in square brackets in Eq. (7) are given by the usual expression $[J_c]=\sqrt{2J_c+1}$. The dipole matrix is similarly transformed

$$\mathbf{d}^{J_{cs}}=\mathbf{X}^\dagger\mathbf{d}^{LS}. \tag{8}$$

So far, nothing has been done to alter the results from those predicted in an LS calculation since this is a unitary trans-

TABLE II. Ne and Ne^+ LS energies.

State		Energy			
		Theory		Experiment[a]	
		Absolute (a.u.)	Relative (eV)	Relative (eV)	Photon energy (eV)
Ne	$2s^22p^6\ ^1S$	−128.725	−22.002	−21.559	0.000
Ne^+	$2s^22p^5\ ^2P^o$	−127.895	0.000	0.000	21.559
	$2s2p^6\ ^2S$	−126.904	26.966	26.912	48.471
	$2s^22p^4(^3P)3s\ ^4P$	−126.885	27.491	27.207	48.766
	$2s^22p^4(^3P)3s\ ^2P$	−126.862	28.118	27.803	49.368
	$2s^22p^4(^3P)3p\ ^4P^o$	−126.761	30.857	30.542	52.101
	$2s^22p^4(^1D)3s\ ^2D$	−126.755	30.021	30.550	52.109
	$2s^22p^4(^3P)3p\ ^4D^o$	−126.747	30.235	30.992	52.481
	$2s^22p^4(^3P)3p\ ^2D^o$	−126.739	31.477	31.147	52.706
	$2s^22p^4(^3P)3p\ ^2S^o$	−126.731	31.672	31.343	52.902
	$2s^22p^4(^3P)3p\ ^4S^o$	−126.730	31.705	31.362	52.922
	$2s^22p^4(^3P)3p\ ^2P^o$	−126.716	31.095	31.518	53.077
	$2s^22p^4(^1D)3p\ ^2F^o$	−126.627	34.511	34.020	55.579
	$2s^22p^4(^1D)3p\ ^2P^o$	−126.599	34.281	34.264	55.823
	$2s^22p^4(^1S)3s\ ^2S$	−126.610	34.981	34.304	55.863

[a]Reference [21].

formation between two representations. However, once the core energies are adjusted to the experimentally observed fine-structure energies, which we outline below within the context of multichannel quantum-defect theory, this unitarity is lost and LS-forbidden symmetries may be populated.

3. Ionic term coupling

Another consequence of including the spin-orbit operator is that Ne^+ ionic states of the same J_c and parity π_c, but different L_cS_c quantum numbers, can mix. This leads to redistribution of scattering flux among open channels and mixing of resonances in closed channels, thereby providing for another mechanism to populate LS-forbidden symmetries. Following the usual method used in the Belfast codes [12,17–19], the relevant term coupling coefficients are computed as follows. First, the nonrelativistic Ne^+ Hamiltonian $\mathbf{H}_{L_cS_c}$ is diagonalized as in Eq. (3),

$$\mathbf{U}^{\dagger}_{L_cS_c}\mathbf{H}_{L_cS_c}\mathbf{U}_{L_cS_c}=\mathbf{E}_{L_cS_c}, \tag{9}$$

giving the L_cS_c target wave functions in terms of the configuration basis

$$\mathbf{\Phi}_{L_cS_c}=\mathbf{U}_{L_cS_c}\phi. \tag{10}$$

The diagonal matrix $\mathbf{E}_{L_cS_c}$ consists of the *theoretical* Ne^+ energies. Since the spin-orbit matrix elements are small (on the order of 10 meV), appreciable mixing between states

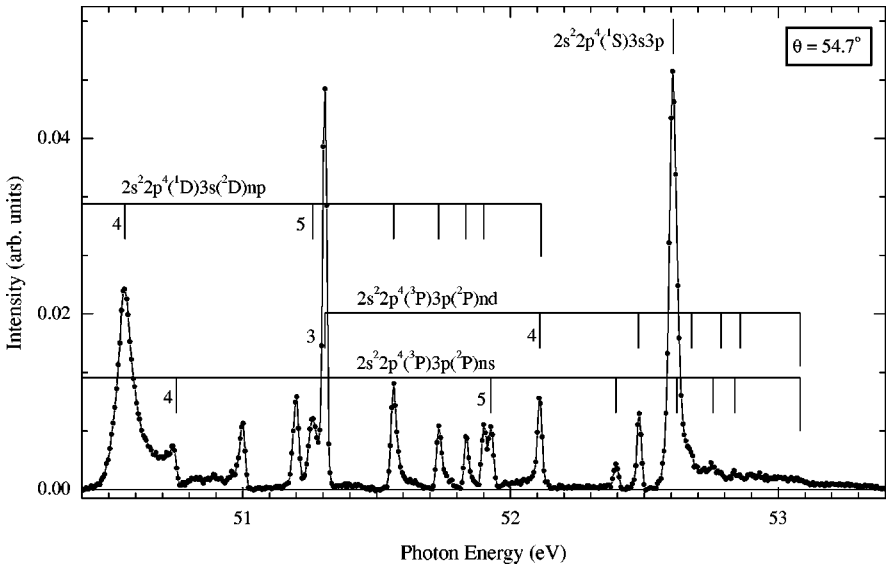

FIG. 1. Experimental cross section (at 54.7°) to the $2s^22p^4(^3P)3s(^2P)$ continua, showing the dominant resonances and tentative classifications in the near-threshold region.

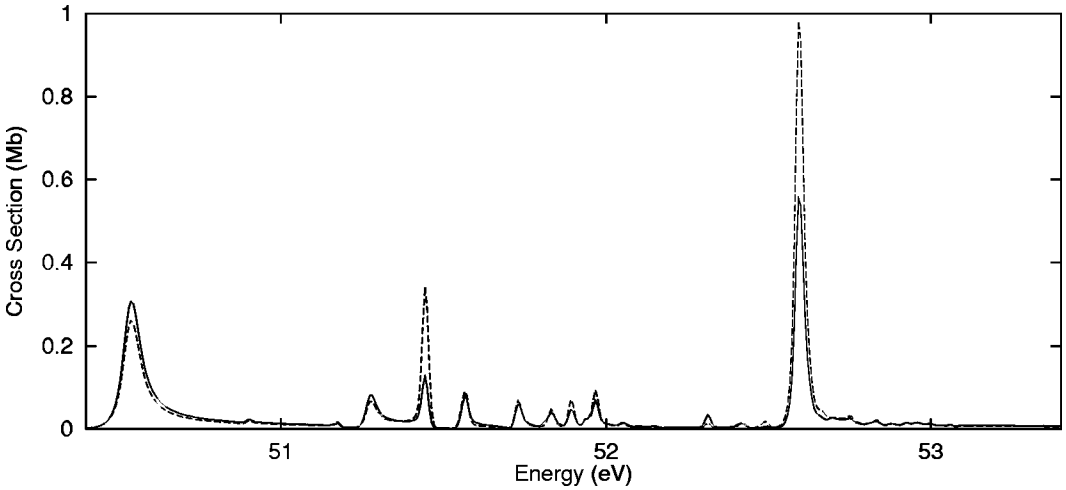

FIG. 2. Theoretical LS-coupled R-matrix results for the cross section to the $2s^2 2p^4(^3P)3s(^2P)$ continuum: solid line, length form; dashed line, velocity form. All results have been convoluted with a 20-meV (the experimental resolution) full width at half maximum Gaussian.

only occurs when the energy separation of the $L_c S_c$ states is comparably small. Due to our energy uncertainties of 0.1–0.5 eV, the mixing is not accurately determined using theoretical energies. We therefore modified the ionic Hamiltonian by the (small) correction

$$\mathbf{H}_{L_c S_c} \leftarrow \mathbf{H}_{L_c S_c} + \mathbf{U}_{L_c S_c}(\mathbf{E}_{exp} - \mathbf{E}_{L_c S_c})\mathbf{U}^{\dagger}_{L_c S_c}, \qquad (11)$$

where E_{expt} are the experimental $L_c S_c$-averaged energies [21]. This ensures that the term coupling coefficients are

TABLE III. Ne^+ experimental fine-structure energies and selected term coupling coefficients.

Level	Designation	Electron energy (eV)[a]	Photon energy (eV)	Mixing
1	$2s^2 2p^5\ ^2P^o_{3/2}$	0.000	21.559	
2	$2s^2 2p^5\ ^2P^o_{1/2}$	0.097	21.656	
3	$2s 2p^6\ ^2S_{1/2}$	26.912	48.471	
4	$2s^2 2p^4(^3P)3s\ ^4P_{5/2}$	27.169	48.728	
5	$2s^2 2p^4(^3P)3s\ ^4P_{3/2}$	27.233	48.792	
6	$2s^2 2p^4(^3P)3s\ ^4P_{1/2}$	27.270	48.829	
7	$2s^2 2p^4(^3P)3s\ ^2P_{3/2}$	27.783	49.343	
8	$2s^2 2p^4(^3P)3s\ ^2P_{1/2}$	27.860	49.419	
9	$2s^2 2p^4(^3P)3p\ ^4P^o_{5/2}$	30.524	52.083	
10	$2s^2 2p^4(^3P)3p\ ^4P^o_{3/2}$	30.552	52.111	$\lesssim$1% of No. 16, $\lesssim$1% of No. 19
11	$2s^2 2p^4(^3P)3p\ ^4P^o_{1/2}$	30.575	52.137	
12	$2s^2 2p^4(^1D)3s\ ^2D_{5/2}$	30.549	52.108	
13	$2s^2 2p^4(^1D)3s\ ^2D_{3/2}$	30.550	52.109	
14	$2s^2 2p^4(^3P)3p\ ^4D^o_{7/2}$	30.886	52.445	
15	$2s^2 2p^4(^3P)3p\ ^4D^o_{5/2}$	30.928	52.487	4% of No. 18
16	$2s^2 2p^4(^3P)3p\ ^4D^o_{3/2}$	30.959	52.518	1.5% of No. 19, 1% of No. 10
17	$2s^2 2p^4(^3P)3p\ ^4D^o_{1/2}$	30.977	52.536	
18	$2s^2 2p^4(^3P)3p\ ^2D^o_{5/2}$	31.122	52.681	4% of No. 15
19	$2s^2 2p^4(^3P)3p\ ^2D^o_{3/2}$	31.185	52.744	1.5% of No. 16, 1% of No. 22
20	$2s^2 2p^4(^3P)3p\ ^2S^o_{1/2}$	31.343	52.902	9% of No. 23
21	$2s^2 2p^4(^3P)3p\ ^4S^o_{3/2}$	31.363	52.922	$\lesssim$1% of No. 10
22	$2s^2 2p^4(^3P)3p\ ^2P^o_{3/2}$	31.513	53.072	1% of No. 19
23	$2s^2 2p^4(^3P)3p\ ^2P^o_{1/2}$	31.529	53.088	9% of No. 20
24	$2s^2 2p^4(^1D)3p\ ^2F^o_{5/2}$	34.017	55.576	
25	$2s^2 2p^4(^1D)3p\ ^2F^o_{7/2}$	34.023	55.582	
26	$2s^2 2p^4(^1D)3p\ ^2P^o_{3/2}$	34.254	55.813	
27	$2s^2 2p^4(^1D)3p\ ^2P^o_{1/2}$	34.284	55.843	
28	$2s^2 2p^4(^1S)3s\ ^2S_{1/2}$	34.304	55.863	

[a]Reference [21].

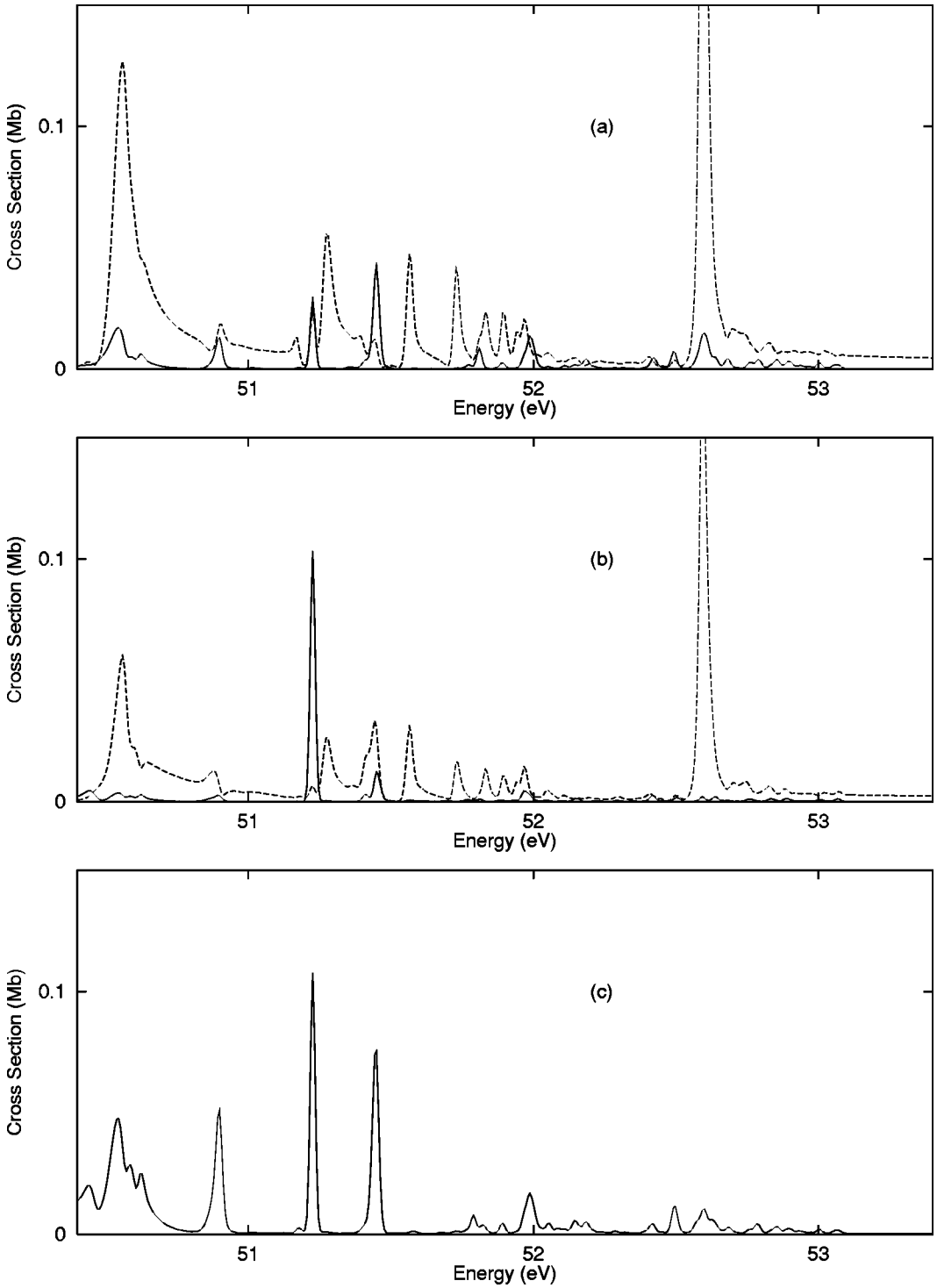

FIG. 3. Intermediate-coupling frame transformation R-matrix results for the partial cross section to various $2s^2 2p^4(^3P)3s$ levels: (a) $^2P_{3/2}$ level for $J_{cs}=1$ (dashed line) and $J_{cs}=2$ (solid line), (b) $^2P_{1/2}$ level for $J_{cs}=1$ (dashed line) and $J_{cs}=0$ (solid line), and (c) sum of all three $^4P_{5/2,3/2,1/2}$ levels (solid line). All solid lines are LS-forbidden contributions.

computed using the physical energy separations. Next we diagonalized the semirelativistic Hamiltonian including the spin-orbit matrix $\mathbf{V}_{so}$:

$$\mathbf{U}_{J_c}^{\dagger}(\mathbf{H}_{L_cS_c}+\mathbf{V}_{so})\mathbf{U}_{J_c}=\mathbf{E}_{J_c}. \tag{12}$$

The J_c wave function with the spin-orbit interaction included is thus

$$\mathbf{\Phi}_{J_c}=\mathbf{U}_{J_c}\phi \tag{13}$$

and, using Eqs. (10) and (13), differs from the L_cS_c wave function by the unitary transformation

$$\mathbf{\Phi}_{J_c}=\mathbf{U}_{J_c}\mathbf{U}_{L_cS_c}^{\dagger}\mathbf{\Phi}_{L_cS_c}. \tag{14}$$

This leads to a transformation of the channels by the matrix

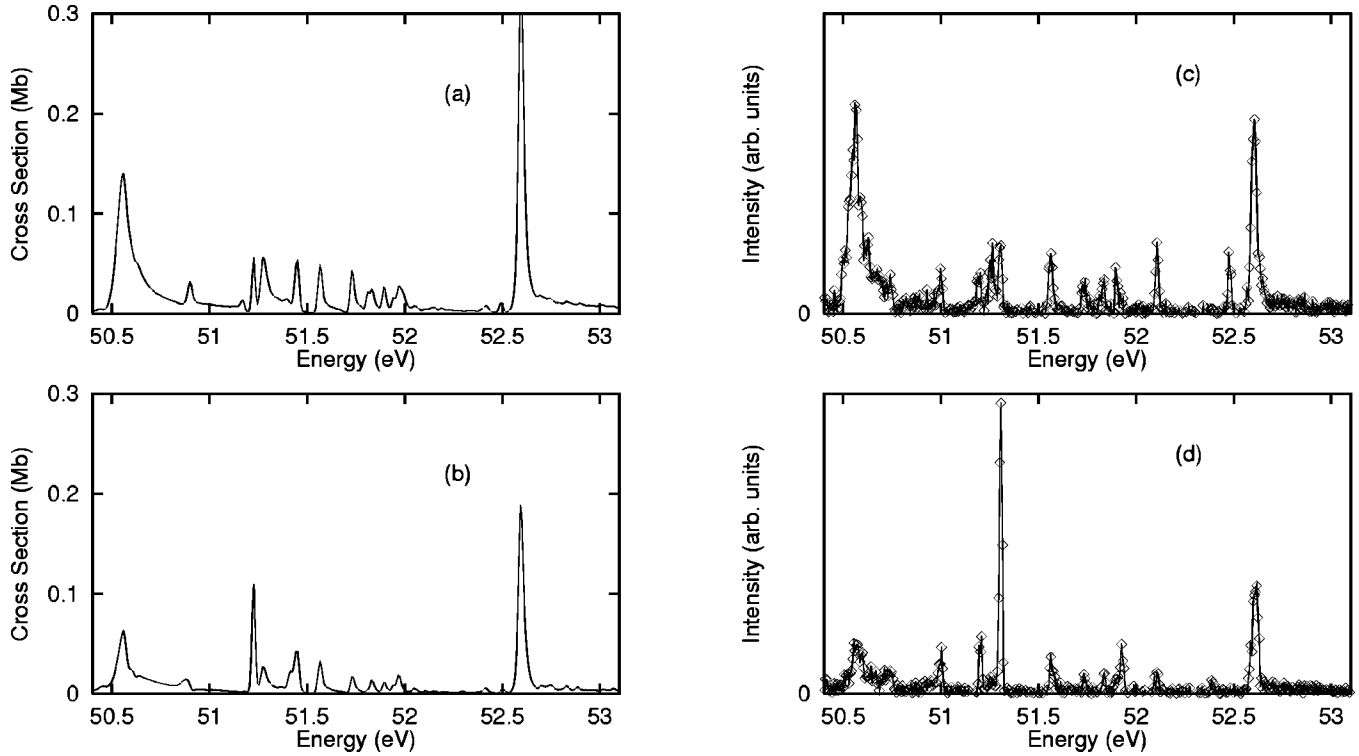

FIG. 4. Theoretical $2s^2 2p^4(^3P)3s(^2P_{3/2,1/2})$ partial cross sections: (a) 3/2 level and (b) 1/2 level. Experimental results: (c) 3/2 level and (d) 1/2 level.

$$(\mathbf{U}_{TC})_{\gamma\delta} = \mathbf{U}_{J_c}\mathbf{U}^{\dagger}_{L_c S_c}\delta_{J_{cs}J'_{cs}}\delta_{ll'}\,. \tag{15}$$

The L_cS_c-J_{cs} transformation matrix $\mathbf{X}$ is therefore modified as

$$\mathbf{X} \leftarrow \mathbf{X}\mathbf{U}_{TC}\,. \tag{16}$$

We point out that the use of term coupling of certain channels, in conjunction with the MQDT frame transformation method, has been used in previous photoionization studies, where they were referred to as ''dynamic'' and ''geometrical'' frame transformations, respectively [22]. This method has also been used quite recently for electron-impact excitation studies [23].

4. Multichannel quantum-defect theory

Following the usual MQDT procedures [24–27], the J_{cs}-coupled reactance matrix is partitioned into open and closed blocks (the J_{cs} superscript will now be dropped):

$$\mathbf{K} = \begin{pmatrix} \mathbf{K}_{oo} & \mathbf{K}_{oc} \\ \mathbf{K}_{co} & \mathbf{K}_{cc} \end{pmatrix}. \tag{17}$$

By transforming and reducing to a physically meaningful subset of open channels [i.e., by requiring that the closed channel solutions have the exponentially decaying form $\mathbf{C}\sin(\pi\nu)+\mathbf{S}\cos(\pi\nu)$], the reactance matrix and dipole matrix are transformed into the *physical* quantities

$$\mathbf{K}^{phys} = \mathbf{K}\begin{pmatrix} \mathbf{1}_{oo} \\ \mathbf{M}_{co} \end{pmatrix},$$

$$\mathbf{d}^{phys} = (\mathbf{1}_{oo} \quad \mathbf{M}^{\dagger}_{co})\mathbf{d}, \tag{18}$$

where

$$\mathbf{M}_{co} = -[\mathbf{K}_{cc} + \tan(\pi\nu)]^{-1}\mathbf{K}_{co} \tag{19}$$

and $\mathbf{1}_{oo}$ is the identity matrix in the open-channel subspace. The elements of the diagonal matrix ν are the effective quantum numbers related to the scattering energy by $E = E_{J_c} - 1/2\nu^2_{J_c}$ and are initially equal for all fine-structure levels belonging to the same LS ionic term. These are then adjusted to the experimentally observed values, giving different phase accumulations for the Rydberg orbitals. The dipole matrices are then transformed to **S**-matrix normalization

$$\mathbf{d}^{phys} \leftarrow (\mathbf{1} + i\mathbf{K}^{phys})^{-1}\mathbf{d}^{phys}. \tag{20}$$

5. Cross section and angular distribution parameter

The dipole matrix yields the photoionization cross section to any final ionic state J_c, which can now be written as an incoherent sum of contributions from each J_{cs},

$$\sigma_{J_c} = \frac{4\pi^2\omega^q}{3c^3(2J_0+1)}\sum_{J_{cs},l} d_{J_cJ_{cs}l}d^{*}_{J_cJ_{cs}l}\,, \tag{21}$$

where $q=1$ (-1) using the length (velocity) forms of the dipole operator. Another important quantity is the angular distribution parameter β. It is defined by the degree of anisotropy in the differential cross section and for linearly polarized light and summing over electron polarizations, takes the form [28]

$$\frac{d\sigma}{d\Omega} = \frac{\sigma}{4\pi}[1 + \beta P_2(\cos\,\theta)], \tag{22}$$

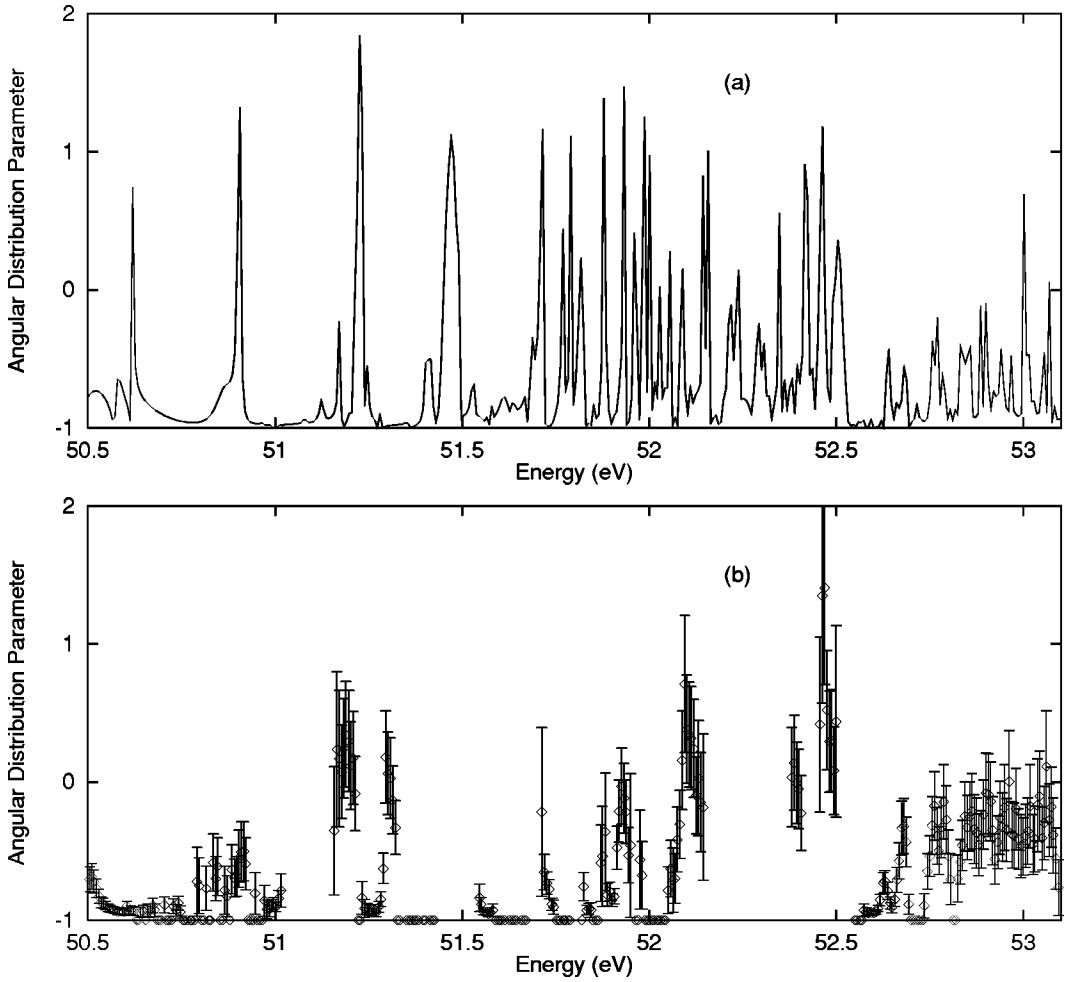

FIG. 5. Angular distribution parameters β for the total ($J_c=3/2,1/2$) $2p^4(^3P)3s(^2P)$ continuum: (a) R-matrix results and (b) experimental results.

where θ is the angle between the photoelectron's momentum and the initial polarization of the photon and $P_2(\cos\theta)=(3\cos^2\theta-1)/2$. Two important consequences of this form of the photoelectron angular distribution are (i) the differential cross section at $\theta=54.7°$, where $P_2(\cos\theta)$ vanishes, is proportional to the integrated cross section σ and (ii) for $\beta=-1$, the differential cross section vanishes at $\theta=0°$. In our J_{cs}-coupling scheme, considering only the present case of photoionization from an initial state $J_0=0$ to a final state $J=1$, this quantity can be computed as [20]

$$\beta_{J_c}=3\sum_{J_{cs},l,l'}(-1)^{J_{cs}}[J]^2[l][l'][2]^2\begin{pmatrix}J_0 & 1 & J\\ 0 & 0 & 0\end{pmatrix}\times\begin{pmatrix}J & 1 & J_0\\ 0 & 0 & 0\end{pmatrix}\begin{pmatrix}l' & l & 2\\ 0 & 0 & 0\end{pmatrix}\begin{pmatrix}2 & J & J\\ 0 & 0 & 0\end{pmatrix} \tag{23}$$

$$\times\begin{Bmatrix}2 & J & J\\ J_{cs} & l & l'\end{Bmatrix}e^{i(l\pi/2-\sigma_l)}d_{J_cJ_{cs}l}e^{-i(l'\pi/2-\sigma_{l'})}d^*_{J_cJ_{cs}l'}\Big/\sum_{J_{cs},l}d_{J_cJ_{cs}l}d^*_{J_cJ_{cs}l}, \tag{24}$$

where σ_l is the usual Coulomb phase shift.

6. Implementation within the Belfast codes

We performed the R-matrix calculations as follows. First, term coupling coefficients were determined, and written to an exterior file, by running the Belfast codes STG1, STG2, and RECUP [12] in Breit-Pauli mode using only one continuum orbital given by the index j in Eq. (1). This minimized the storage requirements. Then a standard LS method was used, with 20 continuum orbitals, to run STG1, STG2, STG3, and STGB. At this point, we ran an extensively modified version of the asymptotic routine STGF, detailed earlier in its use of MQDT for electron-impact excitation [29] and dielectronic recombination [30]. This routine computed the smooth reactance matrices and dipole matrices in Eqs. (17) and (18) and wrote these to a separate file. We wrote a completely separate code to perform the term coupling and LS-J_{cs} recoupling, writing out the new **K** and **d** matrices, and another one to perform the MQDT reduction and the computation of cross sections and β parameters. These are available from the authors upon request.

C. Basis description

To obtain an appropriate set of orbitals for constructing the configurations ϕ_m, we used the program CIV3, optimizing on the same target states as was done earlier [9]. Given this set of orbitals $\{1s,2s,2p,3s,3p,\overline{3d},\overline{4s},\overline{4p}\}$, we then used

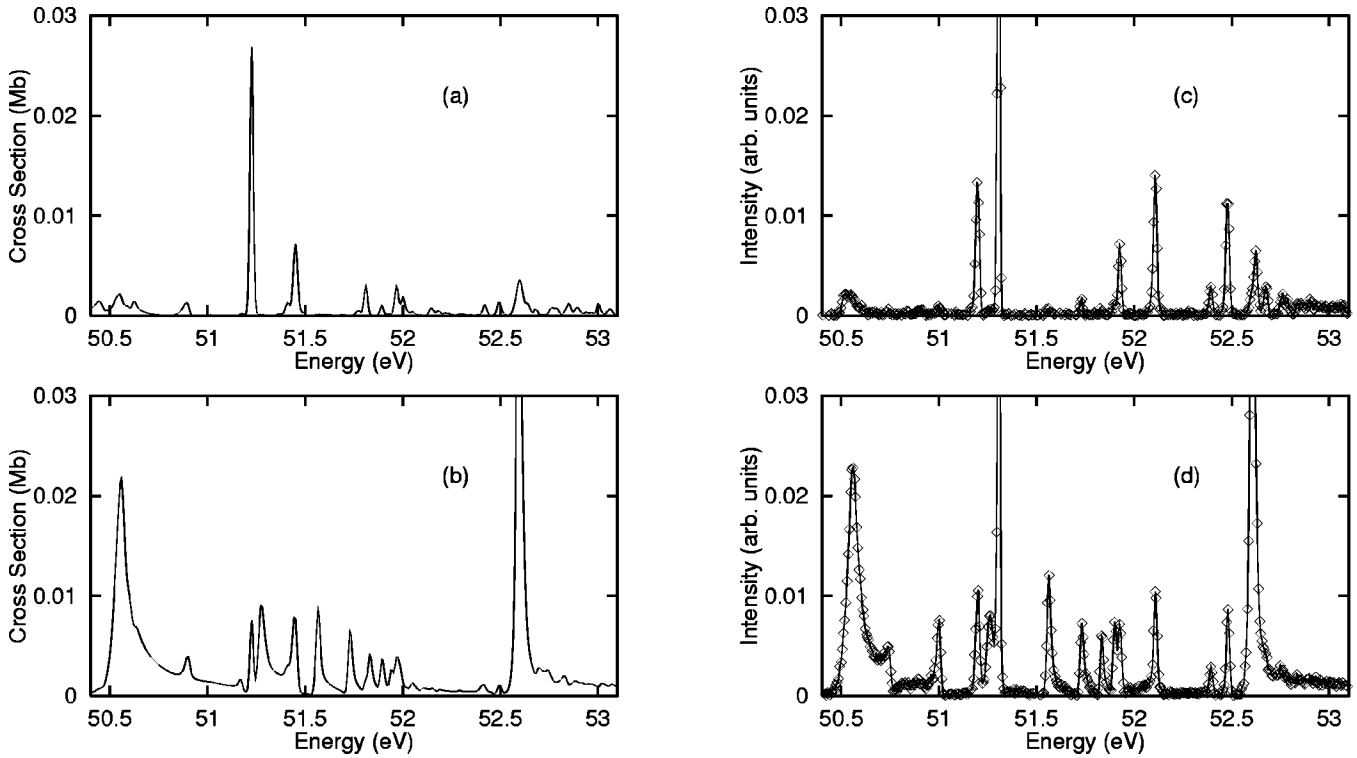

FIG. 6. Theoretical differential partial cross sections to the $2s^2 2p^4(^3P)3s(^2P)$ continuum: (a) $\theta=0°$ and (b) $\theta=54.7°$. Experimental results: (c) $\theta=0°$ and (d) $\theta=54.7°$.

the basis of configurations ϕ_m listed in Table I. Also listed are the neon configurations χ_α that are constructed from these bound orbitals. It was necessary to include all double promotions out of the $2s^2 2p^4 3s3p$ and $2s^2 2p^4 3p3d$ configurations in order to get fairly good energy positions for these resonances, which, as we will see, are strong in the region of interest. The Ne^+ configurations are then used to obtain target wave functions Φ_i and we have chosen to include all the possible LS terms with energies up to about 34 eV relative to the $2s^2 2p^5$ ground ionic state, which should be sufficient for including even the lowest-n resonances in the region of interest. We include states that would not contribute in a pure LS calculation, the quartets and the $^2S^o$ state, since these can couple to LS-forbidden (triplet) symmetries. The energies of these 14 LS states are given in Table II, indicating that, despite the large CI (Table I), the theoretical uncertainty in the relative target energies still ranges from ± 0.1 to 0.5 eV. The target energies were shifted so as to reproduce the experimental resonance positions most accurately. We also adjusted the *absolute* energies of all target states by -0.1 eV since the low-lying resonance positions were found to be at least 0.1 eV lower than the observed ones. The relative shift was also necessary in order to obtain reliable term coupling coefficients. Since the spin-orbit matrix elements are quite small, on the order of 10 meV, significant mixing only occurs for ionic states that are nearly degenerate. The degree of mixing is therefore sensitive to the relative ionic-state positions. These fine-structure levels are given in Table III along with their experimental energies. We also list the term coupling coefficients for those levels that mix by at least 1%, showing that, in particular, the $2s^2 2p^4(^3P)3p(^2P^o_{1/2})$ and $2s^2 2p^4(^3P)3p(^2S^o_{1/2})$ levels mix by nearly 10%.

III. ANGULAR MOMENTUM TRANSFER AND SPIN-ORBIT CONSIDERATIONS

A particularly useful way of viewing the underlying dynamics incorporated in the differential cross section $d\sigma/d\Omega$ in Eq. (22) is to consider the angular momentum transfer $\vec{j}_t$ [31–34]. For photoionization, an incident photon of angular momentum $\vec{j}_\gamma$ ($j_\gamma=1$) is absorbed by an initial atomic state of total angular momentum $\vec{J}_0$, producing a photoelectron of orbital angular momentum $\vec{l}$ coupled to the residual system (the final ionic state of total angular momentum J_c and the *unobserved* photoelectron spin $s=1/2$) of total angular momentum $\vec{J}_{cs}$. Conservation of angular momentum gives the relation $\vec{j}_\gamma+\vec{J}_0=\vec{J}_{cs}+\vec{l}$. The angular momentum transfer, defined as

$$\vec{j}_t \equiv \vec{j}_\gamma - \vec{l} = \vec{J}_{cs} - \vec{J}_0, \tag{25}$$

is a useful quantity because the differential cross section reduces to an incoherent sum of terms associated with the allowed values of j_t [31], that is,

$$\frac{d\sigma}{d\Omega} = \sum_{j_t} \left(\frac{d\sigma}{d\Omega}\right)_{j_t}. \tag{26}$$

The allowed values are $j_t=l-1,l,l+1$ by the first triangular inequality in Eq. (25) and may be further restricted by the second triangular inequality $|J_{cs}-J_0|\leq j_t \leq J_{cs}+J_0$. While the *parity-favored* contributions $j_t=l\pm 1$ have complicated, energy-dependent angular distributions in general, the partial differential cross sections for all *parity-unfavored* transitions $j_t=l$ have the analytic property $(d\sigma/d\Omega)_{j_t=l}\propto \sin^2\theta$ inde-

pendent of energy or, equivalently, $\beta_{unf}=-1$ [32]. One important consequence is that the parity-unfavored contribution to the differential cross section vanishes at $\theta=0°$.

For photoionization from the $2p^6(^1S)$ ground state to the $2p^4 3s(^2P)\epsilon p(^1P^o)$ continuum in LS coupling, the angular momentum transfer is restricted to the single, parity-unfavored value $j_t=l=1$ and the differential cross section vanishes at $\theta=0°$. When spin-orbit effects are considered, on the other hand, L and S are not necessarily individually conserved (i.e., the final state may be one of the triplets $^3L_1$ instead), so that $j_t=\{0,1,2\}$ are all allowed values and the cross section does not necessarily vanish at $\theta=0°$. Thus detection of photoelectrons at $\theta=0°$, which we will report, is an unmistakable indication of LS coupling breakdown and the importance of relativistic effects.

Since $J_0=0$ for the neon ground state, Eq. (25) shows that the intermediate quantum number J_{cs} is identical to the angular momentum transfer $J_{cs}=j_t$. Therefore, we can unambiguously identify the LS-forbidden contributions to the differential cross section by the parity-favored values $J_{cs}\neq 1$. Recoupling between the LS and J_{cs} schemes for the $2s^2 2p^4(^3P)3s(^2P)$ continua of interest, given by

$$\begin{pmatrix} (^2P_{3/2})[1]\epsilon p(J=1^o) \\ (^2P_{3/2})[2]\epsilon p(J=1^o) \\ (^2P_{3/2})[2]\epsilon f(J=1^o) \\ (^2P_{1/2})[1]\epsilon p(J=1^o) \\ (^2P_{1/2})[0]\epsilon p(J=1^o) \end{pmatrix} = \begin{pmatrix} \sqrt{\frac{2}{3}} & \frac{1}{3} & \frac{1}{\sqrt{12}} & -\frac{\sqrt{5}}{6} & 0 \\ 0 & \frac{\sqrt{5}}{3} & -\frac{5}{\sqrt{12}} & \frac{1}{6} & 0 \\ 0 & 0 & 0 & 0 & 1 \\ -\frac{1}{\sqrt{3}} & \frac{\sqrt{2}}{3} & \frac{1}{\sqrt{6}} & -\sqrt{\frac{5}{18}} & 0 \\ 0 & \frac{1}{3} & \frac{1}{\sqrt{3}} & \frac{\sqrt{5}}{3} & 0 \end{pmatrix} \begin{pmatrix} (^2P)\epsilon p(^1P_1^o) \\ (^2P)\epsilon p(^3S_1^o) \\ (^2P)\epsilon p(^3P_1^o) \\ (^2P)\epsilon p(^3D_1^o) \\ (^2P)\epsilon f(^3D_1^o) \end{pmatrix}, \tag{27}$$

shows that the $^1P^o$ symmetry breaks into 2/3 in the $J_c=3/2$ continuum and 1/3 in the $J_c=1/2$ continuum provided the continuum orbitals for these two are assumed to be equal. Deviations from $\sigma_{3/2}/\sigma_{1/2}=2$ are possible to account for through the frame transformation, which yields unequal continuum orbitals, and also through LS-forbidden $J_{cs}\neq 1$ contributions. As another indication of LS-coupling breakdown, the angular distribution parameter β_{J_c} to each fine-structure level can be computed from Eq. (24) as

$$\beta_{3/2}=\frac{-|d_{3/2[1]\epsilon p}|^2+\frac{1}{5}|d_{3/2[2]\epsilon p}|^2+\frac{4}{5}|d_{3/2[2]\epsilon f}|^2+\frac{6\sqrt{6}}{5}\,\mathrm{Re}\{e^{i(\sigma_3-\sigma_1)}d_{3/2[2]\epsilon p}d^*_{3/2[2]\epsilon f}\}}{|d_{3/2[1]\epsilon p}|^2+|d_{3/2[2]\epsilon p}|^2+|d_{3/2[2]\epsilon f}|^2},$$
$$\beta_{1/2}=\frac{-|d_{1/2[1]\epsilon p}|^2+2|d_{1/2[0]\epsilon p}|^2}{|d_{1/2[1]\epsilon p}|^2+|d_{1/2[0]\epsilon p}|^2}. \tag{28}$$

Again, deviations from $\beta=-1$ are due to $J_{cs}\neq 1$ contributions. The separation of the partial cross sections into different J_{cs} contributions thus allows the identification of LS-forbidden, or triplet, symmetries. An easier way to see this, of course, is to note that $\vec{J}_{cs}=\vec{L}_c+\{\vec{S}_c+\vec{s}\}=\vec{L}_c+\vec{S}$, and since we have $L_c=1$, values $J_{cs}\neq 1$ must come from $S\neq 0$, or triplet, symmetries. In general this is not the case, so that it is still useful to label the contributions according to j_t rather than J_{cs}. The contributions from j_t for each partial cross section can be related to the dipole matrices labeled by J_{cs} [33,34].

IV. RESULTS AND DISCUSSION

To highlight the region of complex resonances we are investigating we show, in Fig. 1, the level-unresolved experimental $2s^2 2p^4(^3P)3s(^2P)$ differential cross section at 54.7° [proportional to the integrated cross section; see Eq. (22)]. There are three prominent series: $2p^4(^1D)3s(^2D)np$, $2s^2 2p^4(^3P)3s(^2P)ns$, and $2s^2 2p^4(^3P)3s(^2P)nd$. The last of these was found to exhibit the dominant breakdown of LS coupling in the recent measurements and perturbative calculations [11]. A low-lying $2p^4(^1S)3s(^2S)3p$ perturber is located in the midst of the latter two series at 52.6 eV and the lowest lying $3d$ resonance is located at 51.3 eV. Both of these reside within the R-matrix box, so that they are described primarily by the χ_α configurations. An accurate description of their energy positions thus requires the large configuration expansion in Table I.

We first performed LS-coupled R-matrix calculations for photoionization to the $^1P^o$ final symmetry, shown in Fig. 2. By comparing to the experimental results, it is seen that the dominant resonance features are fairly well reproduced, although certain experimental features, most notably the reso-

nance at 51 eV in the experimental spectrum (Fig. 1), are not reproduced. The theoretical results obtained using the length and velocity forms of the dipole operator agree fairly well too, except on the two resonances $2s^2 2p^4(^3P)3p(^2P)3d$ and $2s^2 2p^4(^1S)3s3p$, noted above.

We next used the intermediate-coupling frame transformation to mix in the other LS-forbidden symmetries $(^3S^o_1, ^3P^o_1, ^3D^o_1)$ and investigated all possible fine structure levels associated with the $2s^2 2p^4(^3P)3s$ designation (see Fig. 3). As discussed earlier, the partial cross sections to the ^2P levels can be separated into contributions from LS-allowed values of the angular momentum transfer $J_{cs}=1$ and LS-forbidden values $J_{cs}=2$ and $J_{cs}=0$ for the $^2P_{3/2}$ and $^2P_{1/2}$ levels, respectively. It is readily seen that the LS-forbidden contributions dominate on certain resonances, indicating that the photoionization-excitation spectrum in this region is not fully characterized by LS-coupling designations. This is further illustrated by the ^4P cross section [summed over all three fine structure levels in Fig. 3(c)], which shows a strong signal on all of the resonances corresponding to $J_{cs}\neq 1$ in Figs. 3(a) and 3(b). We can thus tentatively designate these as triplet in nature. We have not yet attempted to characterize these resonances by their channel indices since we wish to obtain an even better convergence of our atomic description beforehand, which will follow in the future.

We next compare, in Fig. 4, the present $^2P_{3/2}$ and $^2P_{1/2}$ partial cross sections to the experimental results [11], which reported a ratio $r=\sigma_{3/2}/\sigma_{1/2}$ that deviated from the LS-coupling prediction $r=2$. One of the outstanding differences seen in the experiment was for the $2p^4(^1D)3s(^2D)4p$ resonance at 50.6 eV, for which $r\gg 2$. The present theoretical results are only able to reproduce a slight deviation from $r=2$, the difference being due to the larger $J_{cs}=2$ contribution to the $^2P_{3/2}$ cross section in Fig. 3. On the other hand, the $2s^2 2p^4(^3P)3s(^2P)3d$ resonance at 51.3 eV (51.2 eV in the theoretical spectrum) clearly shows a strong LS-forbidden ratio $r<1$, although there are differences between the actual value (since these resonances reside in the R-matrix box, they are least affected by the outer-region frame transformation). Regardless of the quantitative disagreements, the partial cross section shown in Fig. 4(a) is not simply twice that in Fig. 4(b) for many of the features, so that the LS-coupling prediction of $r=2$ no longer holds.

The breakdown of LS coupling is easier to detect, in the present case, by investigating the angular distribution of the differential cross section to the $2p^4(^3P)3s(^2P)$ continuum. As discussed earlier, the angular distribution parameter is identically $\beta=-1$ from the LS-allowed $J_{cs}=1$ contribution alone, for which the differential cross section is expected to be zero at $\theta=0°$. However, the $J_{cs}\neq 1$ contributions lead to the LS-forbidden behavior $\beta>-1$ or equivalently, $d\sigma/d\Omega(0°)>0$. A comparison between the present results and the earlier measurements [11] in Fig. 5 shows that there is qualitative agreement between the two $\beta\neq -1$ profiles. However, this is not the most revealing parameter since, due to the low nonresonant cross section, there is a large uncertainty associated with either the computed or measured value. Indeed, the experimental value given by

$$\beta=\left[\frac{d\sigma}{d\Omega}(0°)\Big/\frac{d\sigma}{d\Omega}(54.7°)\right]-1 \tag{29}$$

was only reported for energies where the cross section differed appreciably from zero. A more quantitative comparison of theory and experiment can be achieved by studying the differential cross section, which we show in Fig. 6. Clearly, many of the strong features at 0° are qualitatively reproduced in our calculation, especially the $2s^2 2p^4(^3P)3s(^2P)3d$ resonance contribution to the 0° cross section. While quantitative agreement is not obtained between theory and experiment, it is clear that the present theoretical method can reproduce significant LS-forbidden results; a more converged description of the resonances in this region should in principle bring the two into better agreement.

The importance of spin-orbit effects is quite remarkable since the spin-orbit forces are so much weaker than the electrostatic forces in the valence shells of neutral neon. However, owing to cancellations among the various direct and exchange electrostatic interactions, near degeneracy among certain of the final states results. Simple perturbation theory arguments [11] show that, despite the smallness of spin-orbit interactions, the near degeneracy of the states allows significant mixing because the energy denominator is so small. It is this near degeneracy that causes the mixing of final states that result in the breakdown of LS coupling.

V. CONCLUSION

We have described the particular details of our intermediate-coupling frame transformation method, as it is incorporated into the Belfast R-matrix codes and as it applies to the case of photoionization excitation of neon to the $2s^2 2p^4(^3P)3s$ continuum. Significant spin-orbit-induced effects were identified by investigating contributions from the intermediate quantum number $J_{cs}\neq 1$ to the partial cross sections of the ^2P ionic levels and also by calculating the LS-forbidden partial cross sections to the ^4P ionic levels. This quantitative assessment of LS-forbidden contributions to the doubly excited photoionization spectrum permits a classification of certain prominent resonances that differs from the standard notation assuming LS coupling, which will be done in the future following a more converged description of these complex resonances. We have also reported the differential cross sections to the $2s^2 2p^4(^3P)3s$ continua, for which fairly good agreement with experiment was obtained in the (LS-forbidden) 0° results. These findings indicate that for an accurate theoretical description of complex resonant spectra, spin-orbit-induced effects should be included since many of the features observed experimentally are found to be LS forbidden.

ACKNOWLEDGMENTS

T.W.G. would like to thank F. Robicheaux for helpful discussions. Z.F. was supported by the U.S. Department of Energy, Office of Basic Energy Science, Division of Chemical Science, under Contract No. DE-FG05-84ER13266. H.L.Z. and S.T.M. were supported by the NSF and NASA.

[1] V. Schmidt, Rep. Prog. Phys. **55**, 1483 (1992).
[2] J. M. Rost, K. Schulz, M. Domke, and G. Kaindl, J. Phys. B **30**, 4663 (1997).
[3] L. Journel, D. Cubaynes, J.-M. Bizau, S. Al Moussalami, B. Rouvellou, F. J. Wuilleumier, L. VoKy, P. Faucher, and A. Hibbert, Phys. Rev. Lett. **76**, 30 (1996); D. Cubaynes, S. Diehl, L. Journel, B. Rouvellou, J.-M. Bizau, S. Al Moussalami, F. J. Wuilleumier, N. Berrah, L. VoKy, P. Faucher, A. Hibbert, C. Blancard, E. Kennedy, T. J. Morgan, J. Bozek, and A. S. Schlachter, *ibid.* **77**, 2194 (1996); S. Diehl, D. Cubaynes, J.-M. Bizau, L. Journel, B. Rouvellou, S. Al Moussalami, F. J. Wuilleumier, E. T. Kennedy, N. Berrah, C. Blancard, T. J. Morgan, J. Bozek, and A. S. Schlachter, *ibid.* **76**, 3915 (1996).
[4] M. Aymar, C. H. Greene, and E. Luc-Koenig, Rev. Mod. Phys. **68**, 1015 (1996).
[5] K. Codling, R. P. Madden, and D. L. Ederer, Phys. Rev. **155**, 29 (1967).
[6] P. G. Burke and K. T. Taylor, J. Phys. B **8**, 2620 (1975).
[7] K. T. Taylor, J. Phys. B **10**, L699 (1977).
[8] T. M. Luke, J. Phys. B **15**, 1217 (1982).
[9] K. Schulz, M. Domke, R. Püttner, A. Gutiérrez, G. Kaindl, G. Miecznik, and C. H. Greene, Phys. Rev. A **54**, 3095 (1996).
[10] B. Langer, N. Berrah, R. Wehlitz, J. Bozek, A. Farhat, and T. W. Gorczyca, J. Phys. B **30**, 593 (1997).
[11] A. A. Wills, T. W. Gorczyca, N. Berrah, B. Langer, Z. Felfli, E. Kukk, J. D. Bozek, O. Nayandin, and M. Alsheri, Phys. Rev. Lett. **80**, 5085 (1998).
[12] K. A. Berrington, W. B. Eissner, and P. H. Norrington, Comput. Phys. Commun. **92**, 290 (1995).
[13] P. G. Burke and K. A. Berrington, *Atomic and Molecular Processes: An R-Matrix Approach* (IOP, Bristol, 1993).
[14] U. Fano, Phys. Rev. A **2**, 353 (1970).
[15] K. T. Lu, Phys. Rev. A **4**, 579 (1971).
[16] C. M. Lee and K. T. Lu, Phys. Rev. A **8**, 1241 (1973).
[17] H. E. Saraph, Comput. Phys. Commun. **3**, 256 (1972).
[18] M. Jones, Philos. Trans. R. Soc. London, Ser. A **277**, 587 (1975).
[19] H. E. Saraph, Comput. Phys. Commun. **15**, 247 (1978).
[20] M. D. Lindsay, C.-J. Dai, L.-T. Cai, T. F. Gallagher, F. Robicheaux, and C. H. Greene, Phys. Rev. A **46**, 3789 (1992).
[21] C. E. Moore, *Atomic Energy Levels*, Natl. Bur. Stand. (U.S.) Circ. No. 467 (U.S. GPO, Washington, DC, 1949), Vol. I.
[22] F. Robicheaux and C. H. Greene, Phys. Rev. A **46**, 3821 (1992).
[23] D. C. Griffin, N. R. Badnell, and M. S. Pindzola, J. Phys. B **31**, 3713 (1998). .
[24] M. J. Seaton, Proc. Phys. Soc. London **88**, 801 (1966).
[25] M. J. Seaton, Rep. Prog. Phys. **46**, 167 (1983).
[26] C. H. Greene, U. Fano, and G. Strinati, Phys. Rev. A **19**, 1485 (1979).
[27] C. H. Greene, A. R. P. Rau, and U. Fano, Phys. Rev. A **42**, 5773 (1982).
[28] A. F. Starace, *Theory of Atomic Photoionization*, edited by W. Mehlhorn, Handbuch der Physik Vol. 31 (Springer, Berlin, 1982), pp. 1–121.
[29] T. W. Gorczyca, F. Robicheaux, M. S. Pindzola, and N. R. Badnell, Phys. Rev. A **52**, 3852 (1995).
[30] T. W. Gorczyca, F. Robicheaux, M. S. Pindzola, and N. R. Badnell, Phys. Rev. A **54**, 2107 (1996).
[31] U. Fano and D. Dill, Phys. Rev. A **6**, 185 (1972).
[32] D. Dill and U. Fano, Phys. Rev. Lett. **29**, 1203 (1972).
[33] D. Dill, Phys. Rev. A **7**, 1976 (1973).
[34] S. T. Manson and A. F. Starace, Rev. Mod. Phys. **54**, 389 (1982).